IOP Conf. Series: Journal of Physics: Conf. Series **796** (2017) 012015 doi:10.1088/1742-6596/796/1/012015

New experimental results on local heat transfer inside a rectangular channel with rib-roughened surfaces

D Fustinoni, P Gramazio, L Vitali and A Niro

Politecnico di Milano, Department of Energy,
Campus Bovisa, Via Lambruschini 4, 20156 Milano, Italy

Corresponding author email: alfonso.niro@polimi.it

Abstract. In this paper we present new experimental results on local heat transfer characteristics of a forced air-flow through a 12-mm-height, rectangular channel of 1:10 aspect ratio, with square-cross-section ribs mounted onto the lower surface. Data are collected on a completely redesigned test section. Specifically, the electric heater is made of very thin copper tracks, in direct contact with the air flow and covering at 97.5% the channel lower surface to guarantee a very uniform heat flux. The copper tracks are laminated onto a 2-mm thick board of FR-4 glass epoxy to provide negligible heat conduction inside the plate and heat losses from its sides. Finally, the channel walls are in XPS and, into the upper one, a double glazing consisting of two 120 mm x 120 mm Germanium windows is mounted to allow optical access to the IR camera and to reduce local heat dispersions. Data here presented refer to convection over 4 mm x 2 mm ribs in transverse configuration for Reynolds numbers, based on the duct hydraulic diameter, ranging between 700 and 8000. Preliminary tests show how the new apparatus has significantly improved the quality, the ease and the quickness of the measurements.

1 Introduction

Forced convection inside rectangular channels with one or more rib-roughened surfaces, with a large variety of configurations, is a subject particularly considered in literature [1-4], as ribs are an efficient and cost-effective way to improve heat transfer in a broad spectrum of applications, ranging from gas-turbine blades cooling to plate compact heat exchangers enhancement. Moreover, channels with only one heated and ribbed surface have been employed as solar air heaters during the last decade [5-8], following the trend of increasing interest around renewable energy technologies.

In this context, local heat transfer measurements over surfaces with complex geometries are very useful from both a conceptual and a practical standpoint, as they provide insight into fluid-dynamic enhancement mechanisms and can be employed as a tool to guide geometry optimization. Moreover, infrared thermography allows a not-intrusive, full-field surveying of the surface temperature with a high spatial resolution, and it can be effectively used to determine the distribution of convective heat transfer coefficient once the local generated and dissipated heat fluxes are known. In fact, several other research group adopted IR thermography-based techniques [9-11], but the experimental procedures are far from being well established, as they strongly depend on the trial setup and on the modeling strategies to calculate the non-convective heat flux components.

Our research group is experienced in both measuring global and local heat transfer in internal geometry [12-13], but local heat transfer, enhanced by square ribs, for transitioning flow regimes, i.e. for Reynolds numbers ranging from 2500 to 25000, need more investigation to characterize the effects of turbulence onset and to identify the flow structures generated by the ribs. These considerations have led to fully redesign our former experimental apparatus and measurement procedures in order to obtain higher precision. In this paper we present the new experimental apparatus, along with the results for the reference flat channel and the configuration with transverse ribs. In both cases, the channel has a 1:10 aspect ratio rectangular channel and only one heated surface, for steady state conditions.

2 Experimental setup

A new experimental setup, which consists of an open loop wind tunnel, has been designed (figure 1) and built aimed at improving the precision of local convective heat transfer coefficient measurements. In particular, the new test section has been thought to reduce dispersive heat flux components from the heater surface, and to reduce the system's thermal inertia. Therefore, the resulting apparatus should allow a higher accuracy in determining the fraction of convective heat flux from the total input, i.e. the known electrical heating by joule effect, and should reach steady-state conditions faster than the previous bulky channel.

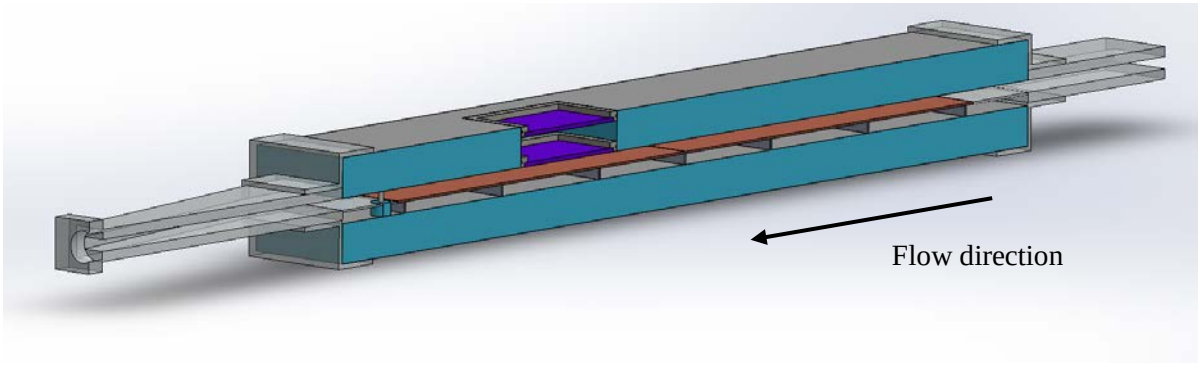

Figure 1. Test section design

In detail, the flow control section, which consists of a 7-stage, 30 kPa-head, 5.5 kW-power blower operating in suction mode and a valve system, has been improved since our previous works with a Hendress Hauser T-Mass 65F15 flow meter for automatic and precise mass-flow readings. Air flows from a convergent inlet and a non-heated entry section, 120 mm wide, 12 mm high, 40 hydraulic diameters long, into a 840 mm long duct with the same rectangular section size, whose external walls are made of 41,6 mm thick extruded polystyrene (XPS), which assures both thermal insulation due to its low thermal conductivity (0.033 W/m/K) and low mass, coupled with a 1 mm HPL laminate skin for damage protection. The channel inner section consists of an aluminum-tape coated upper wall, two Plexiglas side walls and two adjacent 420 mm x 120 mm black-painted heater breadboards on the lower wall, covering the whole test surface.

Each heater is made of a 17.5 μm thick copper circuit deposited on a FR-4 glass epoxy surface, providing a 1.1 Ω resistance, and it is specifically designed to increase planar conduction. The two breadboards are independently powered and controlled with a 5A Carroll & Meynell variac, whose tension is reduced by a 10x, 240 VAC, Legrand transformer. The current provided to each heater is measured by means of a shunt circuit connected to an Agilent 34970A data logger, which is also used to collect tension drops and temperature data. Between the heaters and the bottom external wall, an 11-mm-hight gap provides both thermal insulation and room for wiring.

The optical access for IR surface measurements takes place through a top opening where a 130 mm x 130 mm, 4 mm thick, Plexiglas framed, germanium window is mounted in order to ensure the top surface continuity. However, preliminary heat transfer FEM simulations showed that a single-window

arrangement leads to a discontinuity of thermal properties of the channel wall due to the higher germanium thermal conductivity (about 60 W/m/K), which could affect local measurements with respect to an ideal non-windowed channel. To reduce this effect, a double germanium window arrangement has been designed, with a 20 mm air gap between each glazing. Furthermore, three interchangeable top sections with different opening locations have been made in orderto allow surface measurements in different channel positions.

The IR-camera is a FLIR T650sc, 640 x 480 pixel, microbolometric-type, with a declared NETD of 20 mK at 30 °C, and it is mounted on a Manfrotto tripod with an orientable head. The camera points the test surface at a 20° angle with respect to the normal direction, in order to avoid self-reflections.

The apparatus has also been equipped with several temperature sensors as listed in table 1. In particular, the air temperature is measured with PT100 RTDs, one placed at the channel inlet, and three at the outlet, just behind the test section, for bulk temperature measurements. Each of these is embedded in a vertical-mounted, 2-mm diameter, aluminum cylinders, which provide a physical integral action. The bulk temperature is a weighted average of these three measurements.

T-type thermocouples are employed to measure temperature of germanium window, channel side wall, and channel bottom wall beneath the heater in five spots at 200 mm, 360 mm, 520 mm, 690 mm, and 820 mm, respectively, from the first breadboard edge, as shown in figure 2.

Table 1: thermocouple and Pt-thermometre arrangement

T sensor	Type	Placement
T1	RTD	Inlet temperature
T2, T3, T4	RTD	Bulk temperature
T5	T-type thermocouple	Germanium window, channel-side
T6,T7,T8,T9,T10	T-type thermocouple	Channel wall, beneath the heater

Figure 2. Temperature probes, test section.

Finally, the Plexiglas ribs are laser-carved from a Plexiglas plate and kept in position by Plexiglas rails, a solution that allows quick configuration changes, high placement accuracy, and prevent from gluing on the heater's delicate surface.

3 Data processing and uncertainty analysis

The local convective heat transfer can be estimated by an appropriate modeling of the dispersed non-convective heat flux components, which are based on the experimental measurements.

In detail, the local convective heat transfer coefficient is evaluated as

$$h(x,y) = \frac{q_c(x,y)}{T_w(x,y) - T_b(x)} \quad (1)$$

where $q_c(x,y)$ and $T_w(x,y)$ are the convective heat flux and the temperature, respectively, on the surface test at position x,y, according to the reference system shown in figure 3, and $T_b(x)$ the air bulk temperature. As the channel is operated at constant heat flux, temperature $T_b(x)$ is assumed to linearly vary between the measured values at the test section inlet and outlet. Temperature distribution $T_w(x,y)$

is obtained by IR-thermographic measurements, as will be discussed in detail. Finally, the convective heat flux $q_c(x,y)$ is evaluated as

$$q_c(x,y) = q_{in} - \ q_{kz}(x,y) + \ q_{kxy}(x,y) - q_r(x,y) \tag{2}$$

where $q_{in}=(Q_{el}/A)$ is the heat flux delivered by the electric heater assuming a uniform generation by Joule effect; $q_{kz}(x,y)$ the heat losses from the breadboard back side evaluated by the temperature drop measured across the underlying air gap; $q_{kxy}(x,y)$ the heat flux diffusing inside the copper tracks in *x-y* direction; $q_r(x,y)$ the heat losses by radiation towards the channel walls, and through the germanium windows. With regards to our experimental setup, such terms require further specifications about how they are evaluated, that are illustrated in the following subsections.

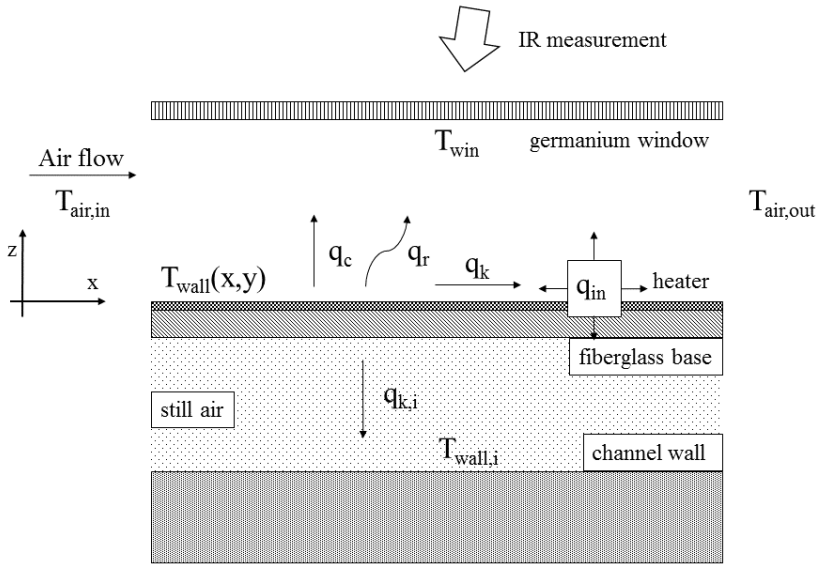

Figure 3. Schematic heat-transfer model of the test section, side view

3.1 Backside breadboard heat losses.

The conductive heat flux towards the lower wall $q_{k,i}$ is calculated by a simple 1D conduction model as showed in equation 3, under the hypothesis of negligible thermal resistance of the fiberglass heater breadboard with respect to the still air layer, and of uniform lower wall temperature. It should be pointed out that radiative heat transfer between the heater plate backside and the channel wall is considered negligible, since their walls have been coated to this end with low-emissivity aluminum foils.

$$q_{kz}(x,y) = \frac{k_{air}}{s_{air}}[T_w(x,y) - T_{si}] \tag{3}$$

3.2 PCB copper tracks conductive heat flux

The heat flux $q_{kxy}(x,y)$ diffusing inside the copper tracks in *x-y* direction is evaluated by means of equation 4, that is obtained by solving a steady-state energy balance inside the copper tracks and assuming negligible temperature variations in their z-direction The derivatives are calculated by interpolating the measured temperature distribution on the surface with a 2D polynomial surface, see paragraph 3.5. The black paint surface layer is supposed to have negligible effect on the surface temperature distribution. Finally, on the basis of FEM simulations heat diffusion inside the breadboard in x-y direction as well as temperature drop across its thickness are assumed negligible too.

$$q_{kxy}(x,y) = k_{Cu} s_{Cu} \left(\frac{\partial^2 T_w}{\partial x^2} + \frac{\partial^2 T_w}{\partial y^2} \right) \quad (4)$$

3.3 Radiative heat flux

The radiative heat flux is calculated for each value of the *x* coordinate with a Matlab script, which solves the radiative heat transfer problem in a 2D cavity with known temperatures, as schematically shown in figure 4. In detail, the germanium window temperature T_{win} is measured and considered uniform due to the high germanium conductivity, the heater temperature distribution $T_w(x,y)$ is known by means of IR measurements, and on the side walls a linear trend between the top and bottom known temperatures is imposed, as found out from FEM simulations in design stage. Heat dispersions due to the high germanium window transmittance in IR region are also taken into account.

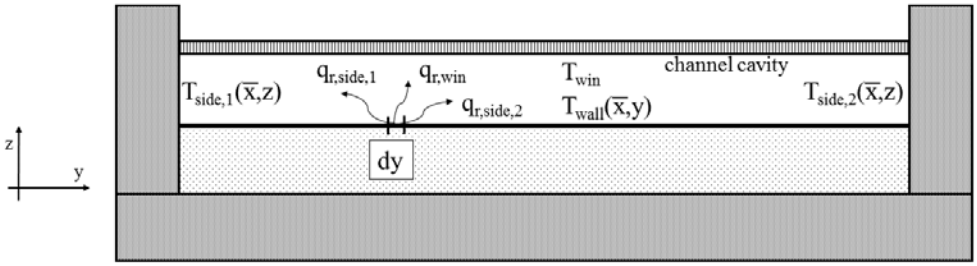

Figure 4. Schematic radiative model of the test section, front view

3.4 Calibrations

As described in the section 3, the sensing instruments adopted in this work are six type T thermocouples, four RTDs, and an IR-camera. Both kind of temperature sensors have been calibrated at once according to the procedure described in detail in [13], i.e., by means of a ThermoHaake heat bath as reference over four uniformly spaced points in the temperature range 30 – 60 °C. The resulting standard deviation is 0.02 K for the thermocouples, and of 0.01 K for the RTDs.

The IR-camera requires a peculiar in-situ calibration in order to evaluate the correct emissivity of the target surface and the eventual loss due to the double germanium window between the camera and the target itself. To this end, a custom test rig has been specifically built. A blackbody, which is a hollow aluminum rod, blackened with the same paint used for the heater surface, is connected to the ThermoHaake thermal bath and heated to fixed temperature. An embedded type T thermocouple measures the blackbody temperature, while two thermocouples record the temperature of the germanium windows. Once stationary conditions have been reached, the target emissivity is set to match the IR camera reading with the measured surface temperature. This procedure has been repeated for three temperatures settings, namely, 40 °C, 50 °C and 60 °C, obtaining a highly linear calibration curve, with $R^2 > 0.999$.

The mass flow meter has been calibrated by the "Istituto Nazionale di Ricerca Metrologica (INRiM)" in Turin, and a 2% accuracy is proven for the range of Reynolds numbers exploited in this research.

3.5 Thermogram processing

A thermogram processing procedure is required (i) to achieve white noise reduction, (ii) to correct the spatial distortion introduced by the angled framing and non-uniform focus over the target surface, and (iii) to allow the computation of the second derivatives, which are needed to estimate the surface conductive heat flux.

The white noise reduction in steady-state conditions is achieved by time-averaging the thermography sequence, obtaining one IR image from a sequence. In particular, the sequences have been acquired both at a 20 Hz frame rate for 1 s, and at a 1 Hz frame rate for 30 s. The output difference between the two acquisition procedures is around the IR-camera NETD, so the quickest has been chosen for this analysis.

The spatial distortion has been corrected by means of a projective transform [14], which restores a perpendicular top-view of the target surface from the angled image, as shown in figure 5. Due to the geometric symmetry of the framed scene, the focus issue has been solved by considering only the top half of the image, and by mirroring it over the centerline. This procedure also overcomes the viewing limitations given by the germanium windows frames. For ribbed surfaces, one surface portion between ribs at a time is taken into account.

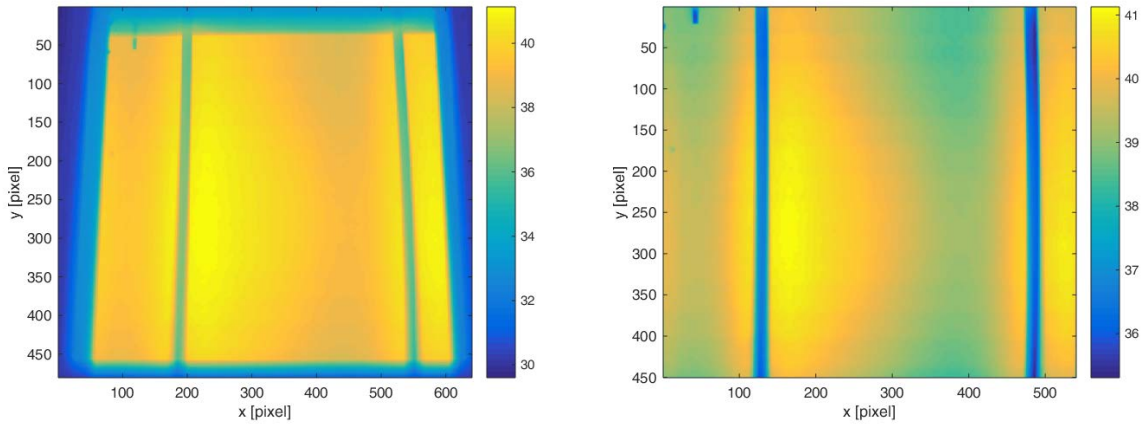

(a) (b)

Figure 5. Time-averaged thermogram, original (a) and after projective transform (b), for the 90° ribbed channel

The last procedure is a filtering of temperature data resulting from time-averaged, projective-transformed, centerline-mirrored and cut thermogram, which allows to calculate the second derivative. To this end, many tests were preliminary carried out with two kinds of techniques, namely, polynomial interpolations in the sense of least squares of degree from 4 to 12 in spanwise direction, and the Wiener filter for 5 different values of mask size applied twice, i.e., a first time to the temperature field and then to its first derivative.

Except for the Wiener filter with mask sized up to 9x9, all tested filtering procedures bring about spanwise distributions of convective coefficient that, in the central zone, i.e., between 15 mm and 105 mm, overlap with differences among them within 5% at most, as well as if compared with the value estimated by the Gnielinski correlation. However, near the sidewalls, the differences between the heat transfer coefficient and the mean value referred to the central zone increase with the order of the fitting polynomial, whereas the values of the heat transfer coefficient obtained by means of the Wiener filter dramatically oscillate with growing amplitude as the mask size increases.

For this reason, the Wiener filter was replaced with a polynomial fitting (4^{th}-order spanwise, 2^{nd}-order streamwise for the flat-surface; 4^{th}-order spanwise, 3^{rd}-order streamwise for the 90° ribbed configuration; R^2 value larger than 0.98 in both cases), resulting in a behaviour of the heat transfer coefficient without inflections, and with values near the sidewalls only slightly increasing above the mean central one.

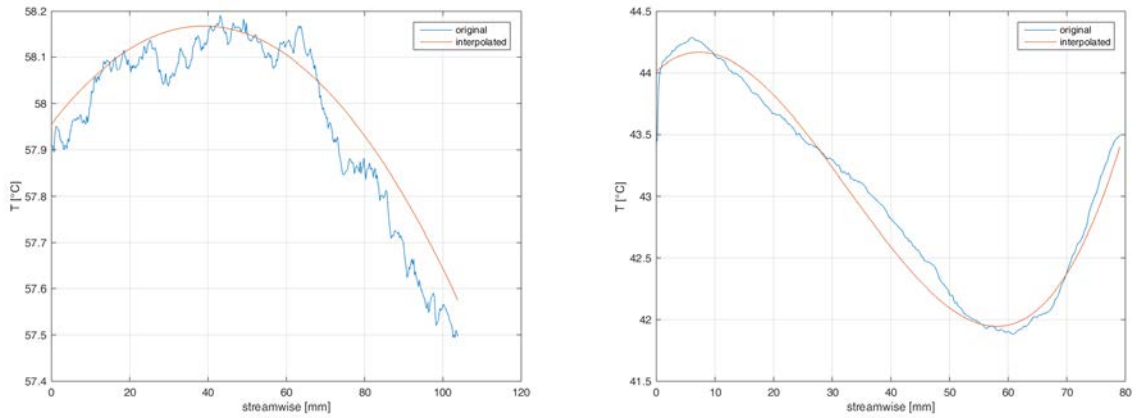

(a) (b)

Figure 6. Streamwise temperature interpolation, flat plate (a) and ribbed (b) configurations

4 Results

In order to assess the experimental apparatus, and to validate the data logging and post-processing procedures, heat transfer coefficients were preliminary measured in a reference configuration, i.e., a rectangular channel with a flat bottom wall. Heat transfer data here presented are for air flows entering the test section at a temperature around 25 °C, for eight Reynolds numbers, based on the duct hydraulic diameter, ranging from 650 to 7280.

Figure 7a displays the time-mean wall temperature field for Re=5400, whereas the corresponding field of heat transfer coefficient *h*, obtained with the procedures previously described, is shown in figure 7b. As can be seen, quite small *h* variations occur in streamwise direction, while spanwise they are within about 10% with respect to its mean value, and for all other Re they never exceed 15%.

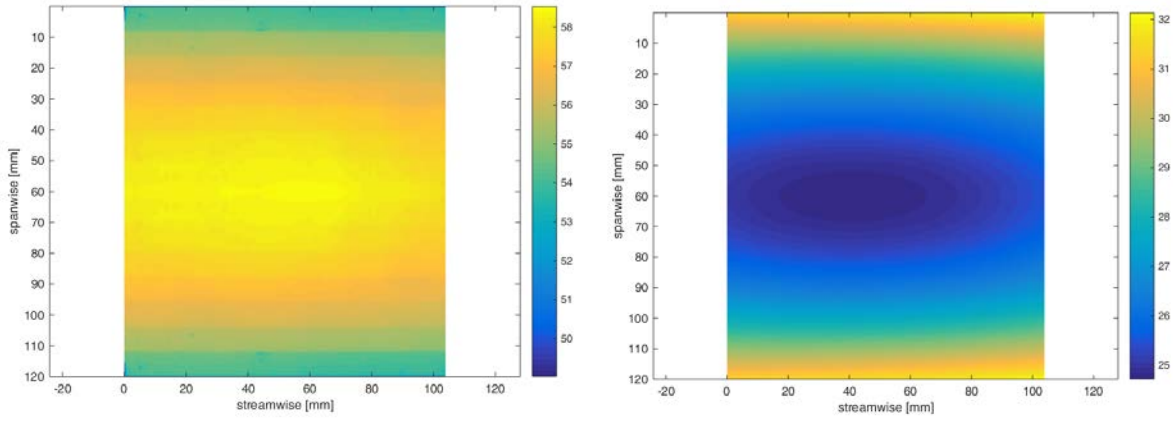

(a) (b)

Figure 7. Temperature (a) and *h* (b) distribution for Re = 5400, flat reference surface

The ribbed configuration has transverse ribs, only on the channel bottom wall, with a square section of 4 mm in side, and a pitch-to-rib height ratio p/e=20. Figures 8a and 8b display the time-mean wall temperature and heat transfer coefficient fields, respectively, for Re=5400. With reference to local effects, the temperature and convective heat transfer fields shown in figure 8 highlight the consequence of the ribs on fluid-dynamics and heat transfer inside the channel. As it can be seen, the temperature distribution clearly shows the rib effect on flow separation as well as on the reattachment zone. In

particular, for the case reported here, the temperature shows a minimum at near one fourth of pitch downstream any ribs, which corresponds also to the region of maximum local *h*.

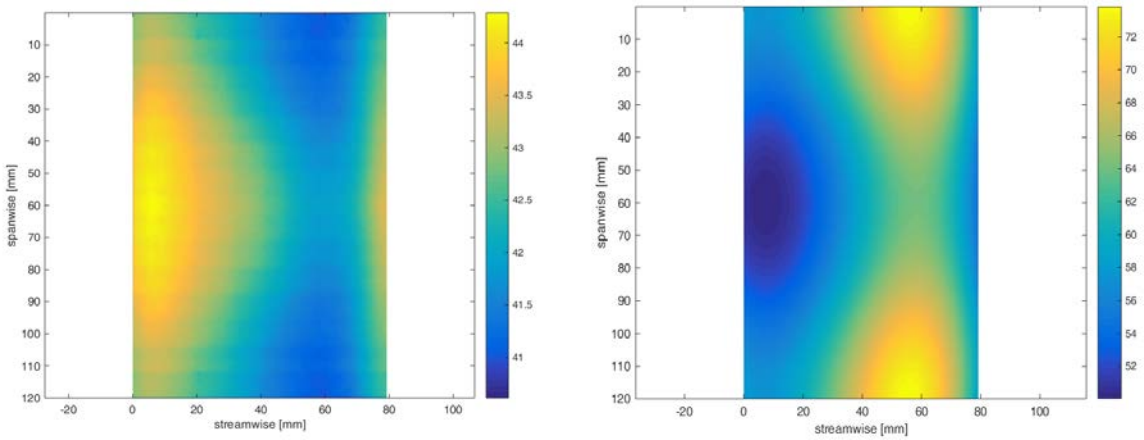

(a) (b)

Figure 8. Temperature (a) and *h* (b) distribution for Re = 5400, 90° rib configuration

Spanwise *h* variations can be still observed, but they continue to be within 15%. We conjecture this outcome is due to a residual conductive effect of side-walls that, however, does not significantly affect the values of the spanwise average heat transfer coefficient.

Indeed, Figure 9a displays the average Nusselt numbers on the considered frame for the flat channel and, as it can be seen, they are in very good agreement with values previously found by our research group in a similar rectangular channel [13] but operated at constant wall temperature. They also agree well with the values calculated by the correlations of Shah and London for Re<2300, and of Gnielinsky for higher values, reported in the same figure as solid lines. Figure 9b displays the average Nusselt numbers for the ribbed wall along with the results previously obtained in a configuration with ribs of the same shape, dimensions and pitch but mounted also on the channel upper wall, operated at constant wall temperature.

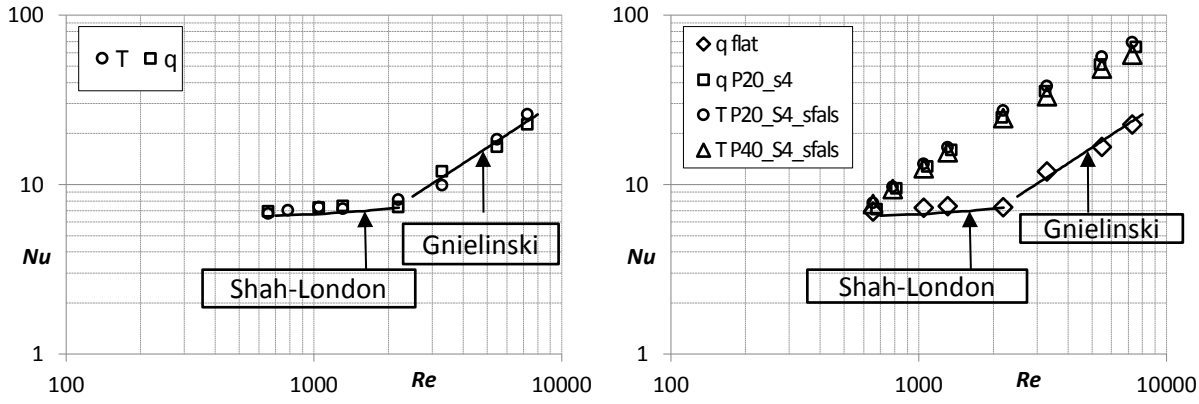

(a) (b)

Figure 9. Temperature (a) and *h* (b) distribution for Re = 5400, flat reference surface

Steady state conditions have been reached in about 1 hour since the test rig activation, which is the expected improvement compared to the previous test rig, which took around 6 hours.

5 Conclusions

In this paper, a new test section and post-processing procedure to measure the local convective heat transfer inside channels has been presented. Preliminary tests show how the new apparatus has significantly improved the quality, the ease and the quickness of the measurements, although the spanwise *h* variations are slightly larger than expected, and hence require further refinements and investigations in order to identify more surely local small scale phenomena. In particular, the insulation around the breadboard and its high planar conductivity give low conductive heat flux components in the balance. Thus, a good estimation of *h* requires a good local radiative heat transfer modeling, especially since the germanium window is spectrally-selective. A great care has been given in this aspect, by measuring the germanium spectral transmittance and by evaluating pixel-by-pixel local view factors as inputs for the estimation of local heat flux, but improvements like 3D effects simulations and dispersion reduction by covering the window with a ceiling having the same temperature as the breadboard are at study. The spanwise *h* variation should also be investigated, either by new FEM analysis of the conduction between the breadboard and the side walls, and by CFD modeling to better understand the spanwise vortex structure. Further work should also take into account more complex rib configurations, and, given the sensitivity and resolution of the IR-camera, smaller turbulators can be tested. Finally, the procedure should be repeated by varying the IR-camera viewing point, to prove the independency of the results from the framing angle and position.

References

[1] Won S Y and Ligrani P M 2004 *Int. J. of Heat and Mass Trans.* **47** 1573-1586
[2] Tanda G 2004 *Int. J. of Heat and Mass Trans.* **47** 229-243
[3] Wang L and Sunden B 2007 *Heat and Mass Trans.* **8** 759-766
[4] Gao X and Sunden B 2001 *Therm. Fluid Sci.* **24** 25-34
[5] Tanda G 2011 *Energy* **36** 6651-6660
[6] Bhushan B and Singh R 2010 *Energy* **35** 202-212
[7] Hans V S, Saini R P and Saini J S 2010 *Sol. En.* **84** 898-911
[8] Patil A K, Saini J S and Kumar K 2010 *Int. J. Ren. Energy Res.* **2** 1-15
[9] Stafford J, Walsh E and Egan V 2009 *Meas. Sci. and Tech* **20** 1-11
[10] Akafuah N K, Hall III C A and Wang T 2004 *Eng. Summer Conf. HT/FED 2004* vol. 1 pp. 367-375
[11] Belmiloudi A 2011 *Heat Transfer - Theoretical Analysis, Experimental Investigations and Industrial Systems* ed. Intech, chapter 21, available online
[12] Ciminà S, Wang C, Wang L, Niro A and Sunden B 2015 *J. of En. Heat Trans.* **22** 29-45
[13] Fustinoni D, Gramazio P, Colombo L P M and Niro A 2012 *J. Phys.: Conf. Ser.* **395** 012042
[14] Szeliski R 2011 *Computer Vision: Algorithms and Applications* ed. Springer, chapter 3, draft available online